This is an open access article published under an ACS AuthorChoice License, which permits copying and redistribution of the article or any adaptations for non-commercial purposes.

ACS OMEGA

http://pubs.acs.org/journal/acsodf

Article

Smartphone-based Fluoride-specific Sensor for Rapid and Affordable Colorimetric Detection and Precise Quantification at Sub-ppm Levels for Field Applications

Sritama Mukherjee, Manav Shah, Kamalesh Chaudhari, Arijit Jana, Chennu Sudhakar, Pillalamarri Srikrishnarka, Md Rabiul Islam, Ligy Philip, and Thalappil Pradeep*

Cite This: *ACS Omega* 2020, 5, 25253−25263

Read Online

ACCESS | Metrics & More | Article Recommendations | Supporting Information

ABSTRACT: Higher levels of fluoride (F^-) in groundwater constitute a severe problem that affects more than 200 million people spread over 25 countries. It is essential not only to detect but also to accurately quantify aqueous F^- to ensure safety. The need of the hour is to develop smart water quality testing systems that would be effective in location-based real-time water quality data collection, devoid of professional expertise for handling. We report a cheap, handheld, portable mobile device for colorimetric detection and rapid estimation of F^- in water by the application of the synthesized core−shell nanoparticles (near-cubic ceria@zirconia nanocages) and a chemoresponsive dye (xylenol orange). The nanomaterial has been characterized thoroughly, and the mechanism of sensing has been studied in detail. The sensor system is highly selective toward F^- and shows unprecedented sensitivity in the range of 0.1−5 ppm of F^-, in field water samples, which is the transition regime, where remedial measures may be needed. It addresses multiple issues expressed by indicator-based metal complexes used to determine F^- previously. Consistency in the performance of the sensing material has been tested with synthetic F^- standards, water samples from F^- affected regions, and dental care products like toothpastes and mouthwash using a smartphone attachment and by the naked eye. The sensor performs better than what was reported by prior works on aqueous F^- sensing.

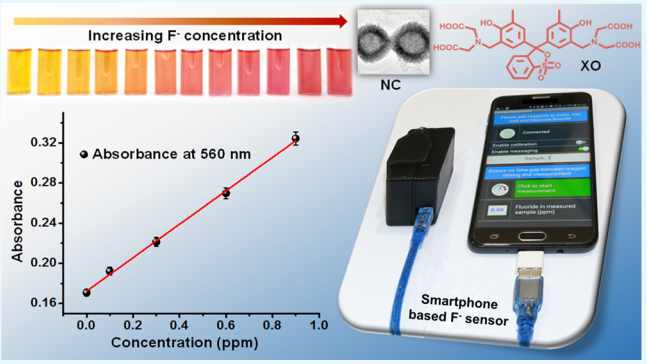

1. INTRODUCTION

Fluoride (F^-), having the smallest anionic radius, highest charge density, and a hard Lewis base character, is a naturally occurring anion in groundwater worldwide.[1] It is a double-edged sword, as on the one hand, it is biologically and medically important for its essential roles in proper growth and maintenance of teeth, hair, nails, and bones and treatment of osteoporosis. While on the other hand, overexposure to F^- can cause dental fluorosis, skeletal fluorosis, kidney, and acute gastric problems.[2] This is because of its unique property of getting easily absorbed in the body, however excreted only slowly. The World Health Organization (WHO) and Environmental Protection Agency (USEPA) have set 1.0−1.5 mg/L (ppm) and 2−4 mg/L, respectively, as its preferred concentration in drinking water.[3,4] The major sources of exposure to fluoride are drinking water, food, dental products, and pesticides. While in USA, artificially fluoridated water (0.7−1.2 mg/L) is supplied to people keeping the necessary dietary intake in mind, on the contrary, population belonging to the contaminated geographical sites get exposed to 6−12 mg/L of F^-.[4] It is estimated that dental caries is the most prevalent of all conditions because of F^- poisoning, with 2.4 billion people globally suffering from caries of permanent teeth and 486 million children from that of primary teeth.[5−7] Hence, it is essential to develop superior analytical methods for F^- sensing and quantification for efficient water quality monitoring.

A number of F^- detection techniques, such as potentiometry, ^{8}F NMR analysis,[8] mass spectrometry,[9] ion chromatography,[9] electrochemical methods,[10] colorimetric methods,[11] and fluorescence-based sensing systems,[11] have been developed over the years.[12] Many of these techniques cannot be used for location-based real-time water quality data collection as they involve cumbersome measurements and are highly dependent on human intervention. Out of them, colorimetric sensing has the advantages of low cost, small size, simplicity,

Received: July 20, 2020
Accepted: September 7, 2020
Published: September 21, 2020

Downloaded via 198.255.135.166 on October 17, 2020 at 17:41:28 (UTC).
See https://pubs.acs.org/sharingguidelines for options on how to legitimately share published articles.

Scheme 1. Schematic Representation of the Smartphone-Based F^- Sensor and Its Sensing Mechanism Using Near-Cubic Ceria@Zirconia NCs and XO Dye

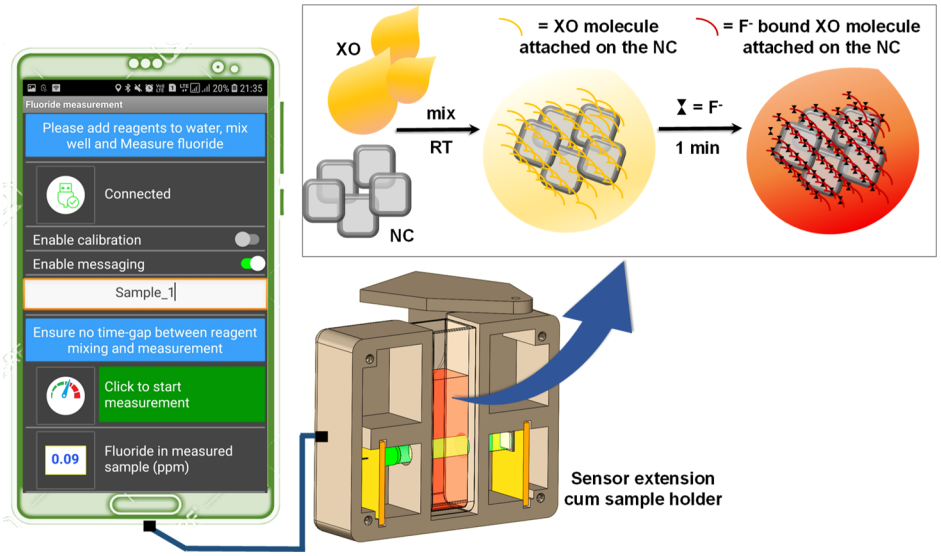

nondestructive in nature, high selectivity, quick response time, and wide applicability in field conditions.[13] Efficient colorimetric probes must have a receptor with a signaling unit which produces a noticeable physical change upon interaction with the analyte, which can be easily read out with the naked eye or an ultraviolet−visible (UV−vis) spectrophotometer.[14] The sensor molecules and F^- have been found to interact via different forces like hydrogen bonding, electrostatic interactions, Lewis acid coordination, chemical reaction, and so forth. Molecular detection based on a specific chemical reaction displays higher selectivity and stability than that based on noncovalent interactions.[14] Recently, many nanomaterials, including gold nanoparticles,[15−18] CeO_2 nanoparticles (CeO_2 NPs),[19] semiconductor quantum dots (QDs), carbon QDs,[20] metal−organic frameworks,[21] micellar nanoparticles,[22] SiO_2 nanoparticles (SiO_2 NPs),[23] graphene oxide (GO),[24] and so on, have been used for aqueous F^- removal and to design a variety of nanosensors because of their large surface areas and well-defined pores, improved solubility, ease of fabrication, low-cost, high sensitivity, and good biocompatibility. The success of a colorimetric method depends largely on the user's perception of colors which may lead to inconsistency in data collection. A few such test kits using lanthanum−alizarin complex, zirconyl-SPADNS reagent, and so on have been commercialized but they largely suffer from high chances of manual errors in interpreting feeble color variations and high cost.[25] Also, they involve serious interferences by anions like sulfate, chloride, and so forth, which compel the use of other chelating reagents, giving rise to expensive and complex multicomponent sensing systems.[26,27] In this direction, systems which are simple, stable, highly sensitive, and selective toward the analyte are of high preference. Moreover, the rapid development of smartphones with various embedded sensors or external sensors (e.g., circuit and probe) integrated with the smartphones for more sophisticated and accurate detection have enabled wide range of applications in environmental and health-related monitoring.[28−30]

We report a smartphone-integrated fluoride sensor platform based on colorimetric detection. The sensor is comprised of core−shell nanocages (NCs) and a chemoresponsive organic dye for accurate, trace level detection of F^- in aqueous medium. Briefly, ethylene glycol-coated ceria@zirconia NCs (CeO_2@ZrO_2 NC) with large surface area and high affinity toward F^- were used as a catalytic platform.[31] The NC system facilitates F^- interaction with xylenol orange (XO) for its specific recognition at sub-ppm levels. A simple smartphone attachment was developed for colorimetric readout using a combination of a light-emitting diode (LED) and a photodiode, which facilitates precise measurement of F^- in water samples as shown in Scheme 1. Using this device, we have demonstrated the quantification of F^- in various real water samples and dental care products within 1 min of reaction time. The device can be operated with an android application which provides instructions to the user as per requirements of the whole process and also provides data storage options such as short message service (SMS) and cloud storage. The consumable cost for F^- estimation using NC-based assay is ∼1 cent/assay.

XO is a well-known indicator, and it has been used as a complexing agent with metals like zirconium/hafnium for determining F^-, but it gives inconsistent results in several cases. The zirconium−XO complex (Zr−XO) shows pH-dependent absorbance values below pH 1.5, and above pH 4, it suffers from serious interference by ions like phosphate and sulfate, and the colored complex has bleaching tendency.[32] Such stability- and selectivity-related issues have been addressed in the following sections. There is a previous report of a mobile-based sensor using a commercial reagent having the Zr−XO complex.[29] In this, the color changes from pink to yellow when F^- ions break the metal ion−dye complex to form colorless zirconium fluoride. The sensor used the camera flash light of the smartphone as an optical source to capture and for RGB analysis of the photograph, making it highly dependent on the quality of the mobile device. There is another report on porous CeO_2−ZrO_2 hollow nanosphere powder of ∼100 nm diameter for F^- adsorption.[33] While ceria−zirconia mixed oxide NPs are widely known for their catalytic properties for various gas-phase reactions and oxygen storage capacity,[34] the present work is the first one on core−shell CeO_2@ZrO_2 NC for colorimetric sensing. In our F^- sensing method, the small

https://dx.doi.org/10.1021/acsomega.0c03465
ACS Omega 2020, 5, 25253−25263

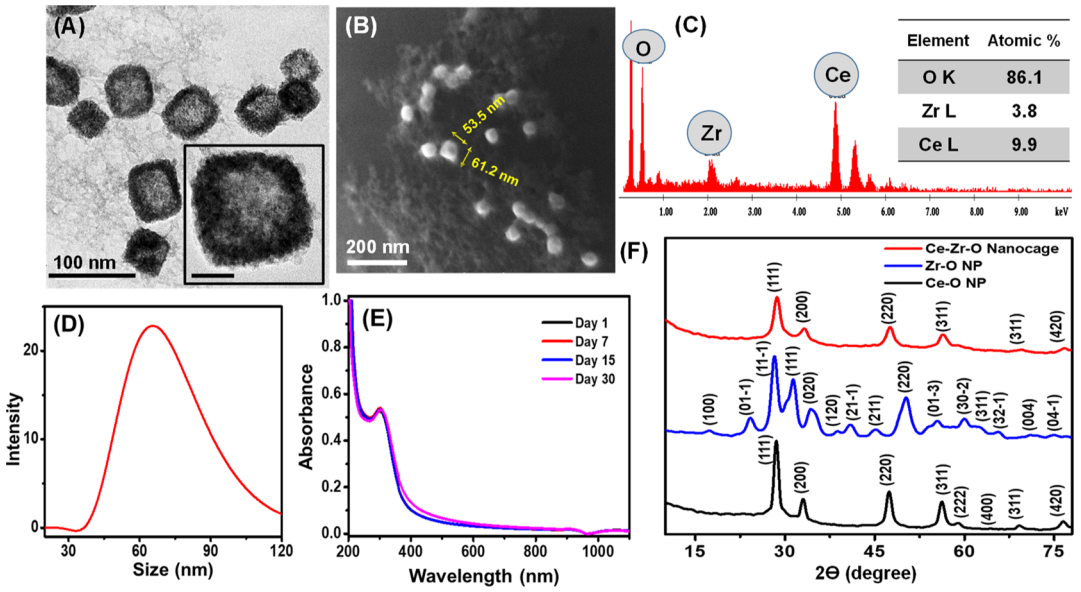

Figure 1. (A) TEM image showing the core−shell structure of CeO_2@ZrO_2 NC with an HRTEM image in the inset, with a scale bar of 5 nm. (B) FESEM image showing a near cube-like structure. Edge length parameters are shown. (C) EDS showing the elemental composition of NCs. (D) DLS data showing the size range. (E) UV−vis data showing the stability of NCs from day 1−30. (F) XRD patterns of CeO_x and ZrO_2 NPs individually and that of CeO_2@ZrO_2 NC.

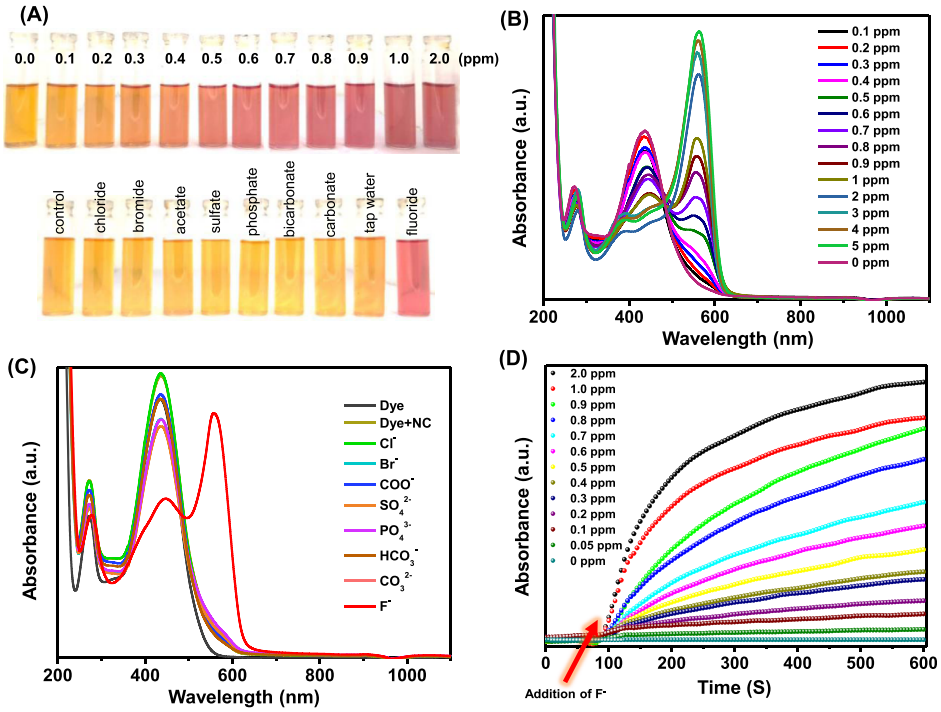

Figure 2. (A) Optical images of the colorimetric changes showing sensitivity of NC−XO system toward various F^- concentrations and its specificity toward F^- as compared to other anions. (B,C) Absorption spectra of the NC−XO system in the presence of various F^- concentrations and in the presence of various interfering anions, respectively. (D) Absorbance vs time plot showing kinetics of the interaction between the NC−XO system and various F^- concentrations responsible for color change.

smartphone extension plays the key role that can be attached to any mobile device irrespective of its quality as the latter is used only as a user interface for calibration and result display. While color is because of XO, the chemistry leading to the color change is mainly because of NC. Sensor optimization experiments revealed that its sensitivity was highly dependent upon the near-cubic shape of the NCs, and both the components (CeO_2 and ZrO_2) were crucial for F^- sensing without directly taking part in the reaction with F^- ions.

2. RESULTS AND DISCUSSION

2.1. Characterization of NCs. CeO_2@ZrO_2 core−shell nanoparticles were prepared by hydrothermal synthesis which resulted in the formation of near-cubic NC having an edge length of 55 ± 5 nm, as shown in Figure 1B,D. Transmission

https://dx.doi.org/10.1021/acsomega.0c03465
ACS Omega 2020, 5, 25253−25263

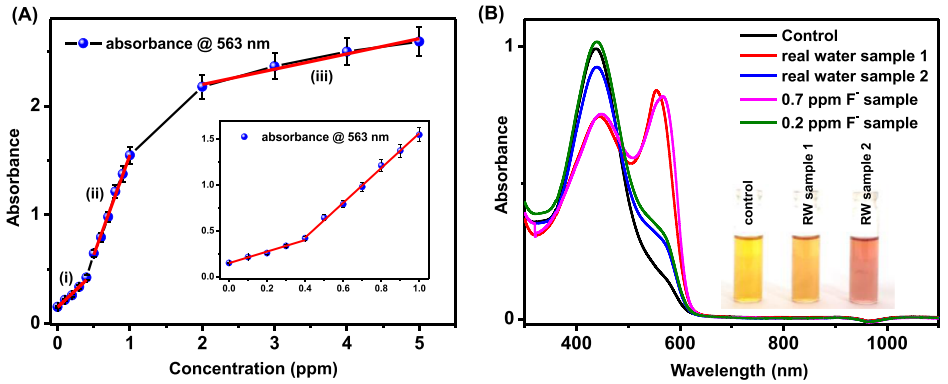

Figure 3. (A) Standard curve of absorbance vs concentration (ppm) for the NC−XO sensor response toward F^- solution (0−5 ppm). Two linear standard regimes in the 0−1 ppm concentration regime are shown in the inset. (B) Absorbance spectra for the sensor for real water samples compared with the response for F^- standards of the same concentration and an optical image of the colorimetric detection of F^- in real water samples (inset).

electron microscopy (TEM) images clearly show the core−shell nature of the NCs in Figure 1A. Large-area microscopic images are shown in Figures S1 and S2. Figure 1C shows the elemental composition of the NC showing that ceria, which is in the core, constitutes more than the amount of zirconia, in the shell. Figure 1E depicts the high stability of NCs over a period of one month when stored in ambient atmosphere, as there is no change in the absorption spectrum of the NCs. The powder X-ray diffraction (pXRD) pattern of NC, as shown in Figure 1F, has a cubic crystal system, which got a little broadened upon the formation of core−shell nanostructures with zirconia but mostly matches with that of the cubic phase of ceria, as it is the major constituent. It shows no similarity with the monoclinic system of zirconia which was synthesized as per the same procedure. A slight shift in the diffraction peak positions (2θ = 28.4−28.8°) could be noted for the NCs, which indicates that along with the particle growth, some compositional changes took place because of interphase mixing. Large-area field-emission scanning electron microscopy (FESEM) images of F-treated NC showed aggregation of particles upon interaction with high concentration of F-ions (Figure S3).

2.2. Testing of the NC−XO Sensor System. Figure 2A shows colorimetric responses of the NC−XO sensor to different concentrations of F^- after mixing for 1 min at room temperature. The solution-phase NC−XO system turns from yellow to rose-red systematically in the presence of various concentrations of aqueous F^-, which is clearly observed with naked eyes because of the stark color difference. The red color intensifies as the concentration of F^- in the sample goes higher, but it gets saturated by 2 ppm F^- for naked eye detection because of the unavailability of active sites of the dye. Change in the color of the NC−XO system is because of change in the molecular structure of the dye. The absorbance peak of the NC−XO system (XO in acidic medium) is at 435 nm, and a broad peak at 560 nm is formed and eventually intensified after the addition of F^- to the system, in the 0.1−5 ppm concentration range. The absorption peaks at 280 and 435 nm of XO are because of the Π−Π* and intramolecular charge transfer (ICT) within the molecule, respectively.[35] While the origin of the new peak at 560 nm is because of nucleophilic addition of F^- to the cationic N-center of the dye leading to adduct formation, reduction in intensity of the 435 nm peak is because of the change in the ICT electronic transition. Absorptivity coefficients were calculated at the absorbance maxima of 1 mM XO before and after analyte interaction, with 1 cm path length. While 1.6×10^3 M^{-1} cm^{-1} is the molar absorptivity for NC−XO at 435 nm before analyte interaction, 0.7×10^3 M^{-1} cm^{-1} (435 nm) and 2.1×10^3 M^{-1} cm^{-1} (560 nm) are the values for NC−XO after interaction with 2 ppm F^-. The sensor system has been tested with several common interfering anions present in groundwater in high concentrations like Cl^-, Br^-, COO^-, SO_4^{2-}, PO_4^{3-}, HCO_3-, and CO_3^{2-} (100 ppm tested), compared with 1 ppm of F^-, as shown in Figure 2C. None of these anions showed absorbance at 560 nm, which proves specificity of NC−XO toward F^-. Figure 2D shows the absorption kinetics of the sensor−analyte reaction. The reaction was monitored till 10 min after F^- solution of various concentrations (0.05−2 ppm) were added to the sensor starting from t = 100 s of initiation. As it is clear from Figure 2D, the rate of change in absorbance is maximum during the first 60−100 s after F^- addition. After that, although the slope keeps increasing, the rate of change decreases and eventually proceeds toward saturation. In view of the observed kinetics, the operating time for the device was set as 60 s. Temperature-dependent kinetics for the same reaction was also studied for 10, 20, 30, and 40 °C (Figure S4) which indicated that higher temperature would accelerate the rate of reaction, resulting in a spontaneous color change.

On the basis of the absorbance data (Figure 2B), a standard curve of absorbance versus concentration (ppm) was plotted which can be used for the quantification of F^- content in water as shown in Figure 3A. In the concentration regime of 0.1−1 ppm, we get two linear plots. Two real water samples were obtained from different F^- affected areas of India, namely, Hanumangarh (Rajasthan, 29.58°N 74.32°E) and Jayanagar (Bangalore, 12.9308° N 77.5838° E), which were tested with the NC−XO system, as shown in Figure 3B. Using the standard curve, the concentrations of those samples were determined and compared with the absorbance spectra of F^- standard solutions of the same concentration, which matched exactly. The colorimetric response NC−XO for real water samples can also be well perceived by naked eyes (inset Figure 3B). We note that the entire calibration curve shows three nearly linear regimes (i, ii, and iii). These regions are interpreted because of the mechanism of the sensing process, which will be discussed later.

https://dx.doi.org/10.1021/acsomega.0c03465
ACS Omega 2020, 5, 25253−25263

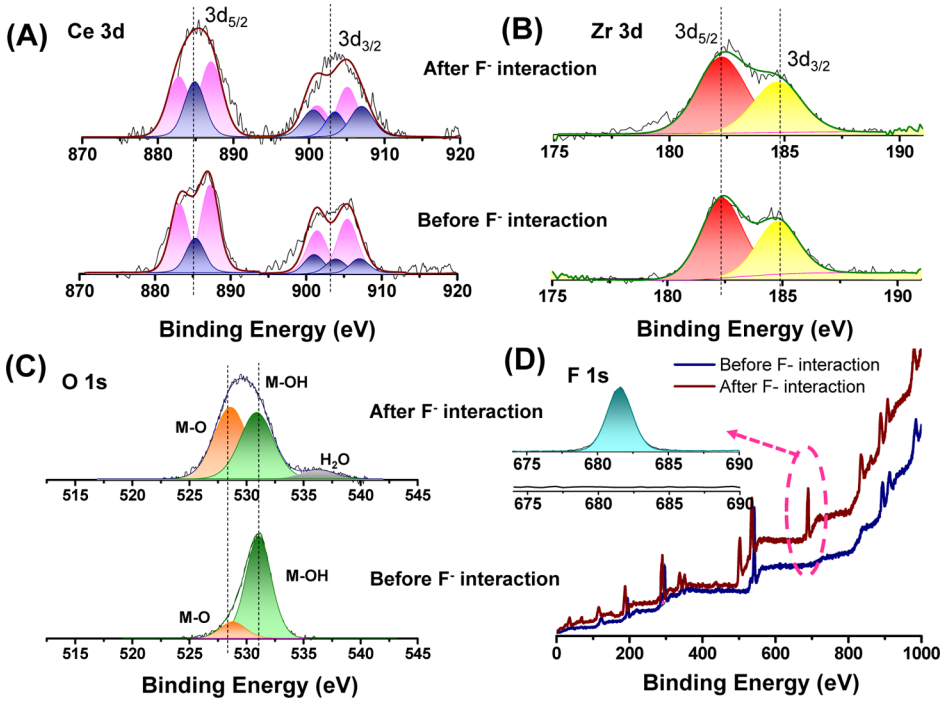

Figure 4. (A) Deconvoluted XPS spectra of (A) Ce 3d, (B) Zr 3d, (C) O 1s, and (D) survey spectra of NC−XO before and after interaction with F^-. The F 1s region is expanded in the inset of (D).

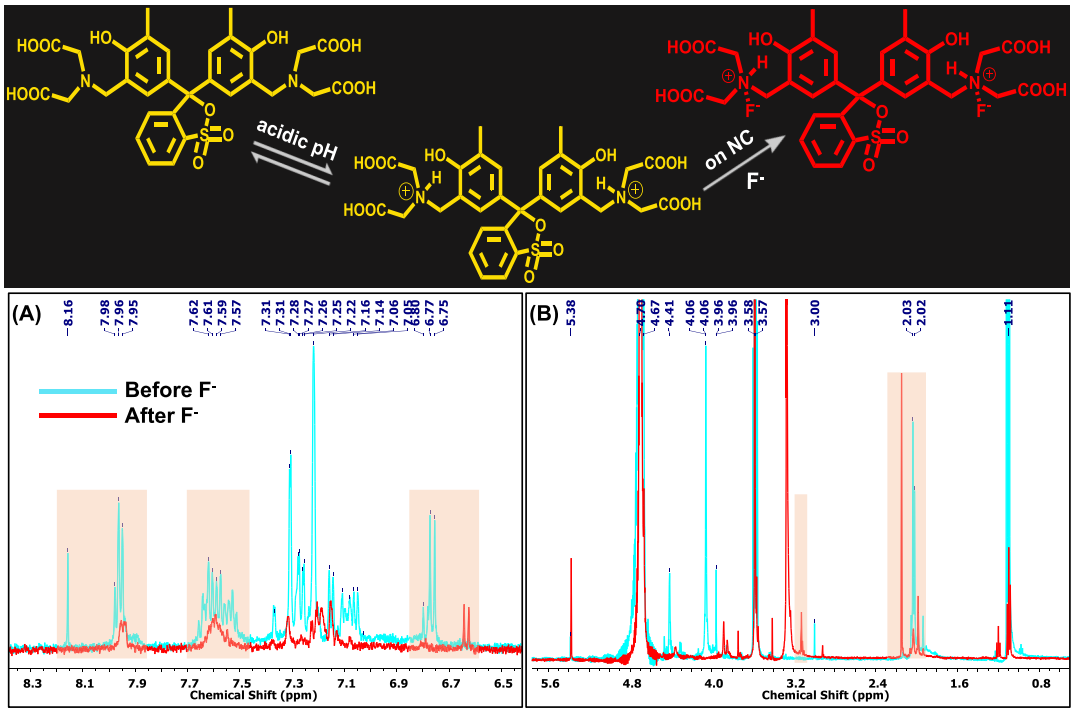

Figure 5. Plausible binding mechanism of F^- with the dye (top). (A,B) shows the zoomed-in regions of overlapping ^1H NMR spectra (500 MHz, D_2O) of (i) XO alone before F^- (in blue) and (ii) NC−XO−F after with F^- (in red) interaction. Specific regions of relevance are highlighted.

2.3. Spectroscopic Studies on the Mechanism of Reaction. X-ray photoelectron spectroscopy (XPS) investigation was carried out to study electronic interactions between the dye-bound NCs and F^- ions. The XPS samples were prepared by drop-casting (i) NC and (ii) NC−XO−F on specimen stubs, followed by air-drying. Deconvoluted XPS spectra in Figure 4A present a complicated Ce 3d profile of mixed Ce^{4+}−Ce^{3+} states for partially reduced CeO_2 specimen. This gives rise to the possible final states, Ce $3d^9$ $4f^2$ O $2p^4$, Ce $3d^9$ $4f^1$ O $2p^5$, and Ce $3d^9$ $4f^0$ O $2p^6$ belonging to CeO_2, mixed with Ce $3d^9$ $4f^2$ O $2p^4$ and Ce $3d^9$ $4f^1$ O$2p^5$ states belonging to Ce_2O_3 because of overlapping of Ce 4f levels with O 2p in the valence band, during photoemission.[36,37] Two sets of spin−orbit multiplets, corresponding to $3d_{5/2}$ and $3d_{3/2}$ contributions show characteristic peaks around 885 and 903 eV, respectively. Set of peaks shaded with blue and pink colors

https://dx.doi.org/10.1021/acsomega.0c03465
ACS Omega 2020, 5, 25253−25263

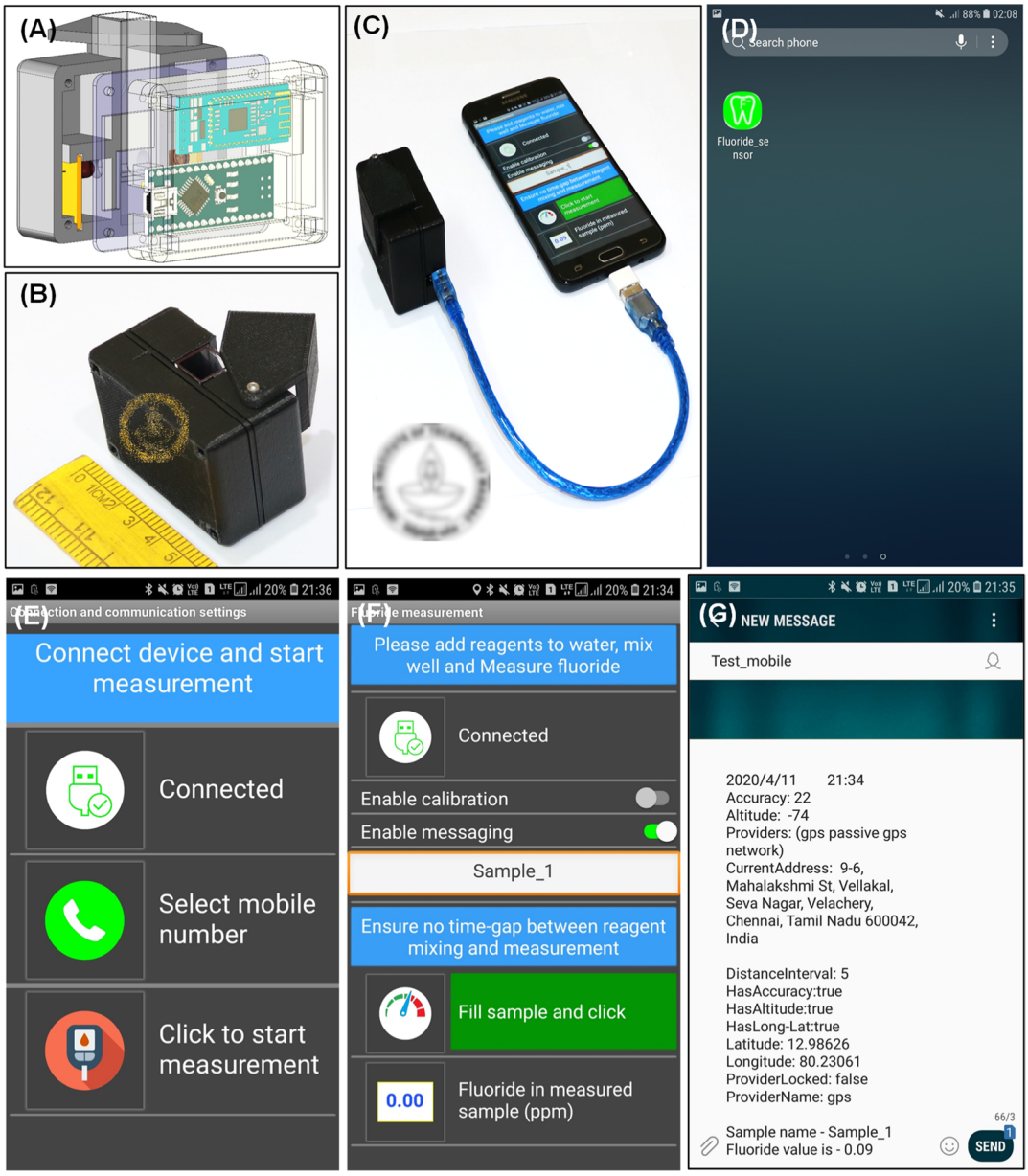

Figure 6. (A) Graphical representation of the extended sensor device cum sample holder. (B) Photograph of the sensor extension cum sample holder. (C) Photograph of the F^- sensor integrated with a smartphone. (D) Icon of the customized mobile application developed for the F^- sensor. (E,F) Screenshot images of the application of a precalibrated sensor for the detection process and for real-time data sharing and storage; and (G) final screen containing the result and the details related to the sample.

correspond to Ce^{4+} and Ce^{3+} oxidation states, respectively. It has been reported that F^- can modulate the surface charge and facilitate electron transfer of CeO_2 NPs.[19,38] An increase in the blue peak area and decrease in the pink peak area upon interaction with electronegative F^- ion indicate oxidation of Ce^{3+} to Ce^{4+}. The electron binding energies located at 182.6 and 184.8 eV in Figure 4B can be attributed to Zr $3d_{5/2}$ and $3d_{3/2}$, respectively, indicating that Zr is in the +4 valence state in the composite, which gets slightly broadened in the presence of F^-. Their comparable intensities and insignificant shift in the binding energy suggest that F^- is not having direct covalent bonding with any of these elements. However, O 1s spectra of NCs in Figure 4C show changes in peak intensities around 528.7 and 530.9 eV upon interaction with F^-. The decrease in intensity of M−OH is because of the attachment of dye with the −OH groups of the NCs and F^- ions interact directly with the dye and not with the core−shell species, which is further proven by NMR analysis. However, addition of the dye to the parent NC increases the overall amount of O in the sample leading to the increase of M−O peak intensity. The XPS survey spectrum (top) in Figure 4D shows the emergence of the F 1s feature after the NCs got exposed to F^- in solution.

To further understand the F^- ion binding mechanism with the dye, we have studied ^1H NMR for XO alone (i) and the NC−XO−F system (ii). Figure 5A,B shows the zoomed-in regions of overlapping ^1H NMR spectra of XO before and after fluoride addition, for clarity. The decrease of signal intensity of (ii) in the aromatic region of the F^- attached XO is because of its interaction with CeO_2@ZrO_2 NC having high electron density, which suggests binding of the dye with NC. The decrease of two COO−H proton integration peaks at the 7.9−8.3 ppm region of (ii) suggests that the dye gets attached to

https://dx.doi.org/10.1021/acsomega.0c03465
ACS Omega 2020, 5, 25253−25263

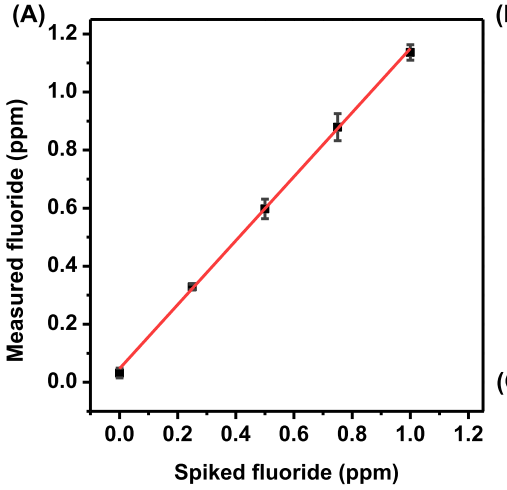

(B)

Sample	F⁻ conc. by device (ppm)	F⁻ conc. by ISE (ppm)
RW 1	0.19 ± 0.02	0.22
RW 2	0.70 ± 0.02	0.70
TP 1	0.17 ± 0.02	0.19
TP 2	0.16 ± 0.02	0.17
MW	0.06 ± 0.02	0.07

(C)

Sample	TP 1	TP 2	MW
Reported	1000	970	360
Obtained	850	800	300

Figure 7. Response characteristics of the designed smartphone-based fluoride sensor device. (A) Device response curve for the lower level of spiked F^- concentrations in the range 0−1.2 ppm. (B) Device output for various real water samples and dental care product samples in the solution phase. TP1, TP2, and MW samples were diluted 5000 times for analysis. (C) F^- concentration in the as-received dental care products (all values are reported in ppm). See the text for the description of samples.

NC by a condensation reaction of −COOH (from dye) and −OH (from NC), by eliminating a water molecule. The alcoholic proton peaks at 6.75 ppm of the dye in (i) got shifted to 6.62 ppm (ii), indicating the shielding of these protons after subsequent binding to NC and F^-. As XO is acidified during the reagent preparation, addition of proton with each of its nitrogen centers leads to the formation of cationic centers, and this proton peak comes at 3.13 ppm as a singlet peak. Deshielding of the peak at 2.15 ppm in (ii) because of four CH_2 protons is because of the close proximity of cationic nitrogen center and F^-. It was noted that F^- addition to the cationic nitrogen did not have any influence on the electron density of the aromatic part. Figure 5 also shows the mechanistic approach of F^- addition to XO. Approach by the small F^- ion to the sterically crowded tetravalent cationic N-center is the main reason of its selective sensing ability. The sensor is stable and works well with water samples of wide pH range, till pH 10.5 (Figure S7). However, beyond pH 11, the dye undergoes chemical transformation to give violet color, even in the absence of F^- in the medium. To confirm this, ^{1}H NMR of the resultant violet sample was measured which did not match with that of NC−XO−F, as shown in Figure S9. The linear regimes in the standard curve, as shown in Figure 3A, are because of the change in reaction rates depending upon the availability of the amount of cationic N-centers to interact with F^- ions. Figure S8 shows full-length overlapping ^{1}H NMR spectra of NC−XO before and after interaction with F^-.

The IR spectrum of the NC−XO system (Figure S5) shows slight shifts in the C−O and C═O stretching frequencies at 1078 and 1653 cm^{-1} to higher wavenumbers upon interaction with F^-.

2.4. Development and Testing of a Smartphone-Based Sensor Device. Color changes in the NC−XO system is easy for readout with naked eyes. However, when it comes to distinguish color differences at lower concentrations, a precise and error free readout method is required. To enable this, a smartphone-enabled fluoride sensing device has been designed. Instead of laboratory measurements which are mainly electrode-based or focused on the UV−vis spectral scan, principle of the measurement using this device is based on monitoring the initial kinetics of the change in absorbance of the NC−XO system. Unlike a spectral scan or single-point absorbance measurement, kinetics-based scan minimizes manual errors because of variation in time taken for sample preparation. This is possible because initial rate of change of absorbance is constant and almost linear for ∼100 s after F^- addition, as shown in Figure 2D. Because of this, rate of change measured within the initial ∼60 s time window remains constant for a specific F^- concentration.

The black-colored device was made by 3-D printing the polylactic acid polymer with 1.75 mm feed extruder using Dreamer Flashforge 3D printer. To lower the cost of the device, additional optics and use of sophisticated optical filters have been avoided. Instead of using a collimation lens, already collimated 565 nm LED (TLHG5800) with a typical luminous intensity of 700 mcd at 2.4 V has been used for illuminating the sample. For signal collection, a photodiode (TEMD5510FX01) with angle of half sensitivity ∼65° has been used so that signal from larger area can be collected without applying any focusing lens. The selected photodiode has spectral sensitivity in the region of 430−610 nm which is suitable for signal collection at 565 nm. LED and photodiode were interfaced with the smartphone using the Arduino-nano microcontroller and HC05 Bluetooth communication board (Figure 6A,B). However, to avoid battery usage, the device was powered through On-The-Go cable connected with the nanoboard (Figure 6C). A plastic cuvette was used for ease of handling and safety during field measurements. An android application "Fluoride_sensor" was developed using the MIT app inventor 2 program to operate the device.[39] App is designed to work in a few simple steps based on the requirement of one time calibration before measurements. It is self-instructive as it informs user the next steps to be performed during the measurements. Typical workflow involves the following steps: click on app icon, connect with the device via bluetooth, enable calibration, select SMS options for data sharing, sample loading as per the instructions prompted by app, and finally, the recorded data (along with other relevant information) appears as SMS on the screen (Figure 6D−G, respectively). Screenshots of the workflow are provided in Figure S10. During measurements, mixture of 500 μL of NC and 1 mM XO 1:1 (v/v) ratio was loaded into the

https://dx.doi.org/10.1021/acsomega.0c03465
ACS Omega 2020, 5, 25253−25263

Table 1. Comparison of Performance Parameters between Various Studies for the F^- Sensors

Sl no.	colorimetric probe	medium	detection range (ppm)	LOD (ppm)	reaction time (min)	refs
1	gold nanoparticles	DMF/phosphate buffer	2.3−28.4	2.3	15	42
2	gold nanoparticles	aqueous/EDTA	0.5−7	0.4	240	43
3	sensors based on benzohydrazide	DMSO	na	0.5	na	44
4	PAA−gold NPs/Al^{3+}	Aqueous	0.1−2.8	0.04	10	45
5	boronic acid molecular sensor	Aqueous	0.1−1.5	0.1	na	46
6	ceria nanoparticles	aqueous/ABTS + acetate buffer	0−1.9	0.01	30	47
7	GO-SPS	aqueous/Tris-HCl buffer	0.1−1.9	0.01	30	48
8	Akvo Caddisfly	aqueous	0−2.0	0.1	1	29
9	Pocket Colorimeter II for fluoride (Hach) [zirconium-SPADNS]	aqueous	0.1−2.0	0.1	na	49
10	CeO_2@ZrO_2 NC−XO	aqueous	0.1−5.0	0.06	1	this work

cuvette to which 2.5 mL of water sample need to be added. A simple three-point calibration can be done using 0, 0.5, and 1 ppm fluoride samples in deionized water. If no calibration is performed, the app uses fitting parameters from the previous calibration data.

The sensor device were repeatedly tested with various lab-prepared and field-collected fluoridated aqueous samples and dental products. Absorbance was also recorded for the response of NC−XO with the same samples, as shown in Figure S6. Two real water samples RW1 and RW2 were collected from the field in states located at two different parts of India, while dental care products included two toothpastes (TP1 and TP2) and a mouthwash, commercially available. Fluoridated toothpastes are used globally to ensure adequate fluoride bioavailability in the oral cavity during tooth brushing and their fluoride content must be chemically free and not bound with the abrasive used in the toothpaste formulation. So, the free fluoride content should be regularly checked in these products. For our analysis, the environmental water samples were having TDS values of 600−800 ppm that showed no interference with the F^- measurement. However, water samples having higher turbidity and TDS > 2000 ppm can be pretreated by passing through a prefilter to get suitable sample for F^- estimation. The dental care products were dissolved in water as per the reported procedure, and the resulting solutions were tested by the sensor device.[40,41] Before testing the samples, the device was calibrated and tested for various F^- concentrations to check its accuracy which is shown in Figure 7A. Each of the samples were tested by keeping reaction time as 1 min. The F^- content in each of them was also measured with the ion-selective electrode (ISE), which is applicable for only one specific target ion, for performance comparison, as shown in Figure 7B. The sensor parameters have also been compared to those of the reported materials and commercial sensors in Table 1. It clearly shows better performance in terms of limit of detection (LOD), concentration range of detection, and reaction time than most of the reported sensors.

To understand the importance of the choice of the sensing material in terms of its composition and shape, control experiments were performed with the zirconium−XO complex,[29] ZrO_2 NP−XO, CeO_2 NP−XO, and spherical CeO_2@ZrO_2 core−shell−XO systems. Their colorimetric response toward 0, 0.1, 1, and 10 ppm F^- were observed by the naked eye, as shown in Figure S11. While the zirconium−XO complex showed slight color change from pink to its lighter shade at 10 ppm, ZrO_2 or CeO_2 nanoparticles with XO systems did not show any significant color change even till 10 ppm. Instant and profound colorimetric response was observed in the case of the spherical CeO_2@ZrO_2 core−shell−XO system, showing extremely high reactivity toward F^- but regulating its rate of reaction was found difficult. Comparing these outcomes, it was concluded that not only the presence of both ceria and zirconia in the nanoscale regime was essential to detect lower F^- concentrations, but the surface area of the nanomaterial is also an important factor for the selection of a suitable sensing material. Near-cubic CeO_2@ZrO_2 NCs showed the optimum reaction kinetics and sensitivity; hence, they were chosen for the F^- sensor. We believe that other nanoshell shapes such as spheres will also be effective in this context.

2.5. Potential Nanoparticle Toxicity. Two major considerations for NP toxicity are (1) size relative to their bulk counterparts and (2) mechanisms associated with capping agents leading to their uptake in biological systems. Generally, because of smaller sizes (and thus greater reactivities) of NPs, they are considered to lead to higher toxicity.[50] It is reported that handling dry powders (of nano cerium oxides), dry aggregates, and consolidated powders or granules have greater potential for dermal and inhalation exposure on workers than dispersions.[51] Also, the application of stabilizers prevents agglomeration-induced toxicity by increasing the stability of the suspension.[52] In our case, NCs of less than 75 nm size have been synthesized with the capping of ethylene glycol, resulting in stable and uniform ethanolic dispersion of NPs. In addition, they are used for sensing experiments in small quantities (125 μL of dispersion having about 80 μg of nanomaterials for each test), making their impact on environment less significant. However, the resultant mixture post individual tests can be stored in a leak-free container till it becomes some quantity. Then, the mixture containing CeO_2@ZrO_2 nanoparticles and adsorbed XO dye can be treated with H_2O_2 for dye degradation by chemical oxidation process, at room temperature. The degradation efficiency of peroxide is expected to be higher because of catalytic activity in the presence of the CeO_2@ZrO_2 nanoparticles, as per literature.[53] On keeping the treated mixture as it is for a week, the adsorbed peroxide over the surface of the nanoparticles would diffuse into the aqueous bulk solvent giving a clean nanoparticle surface. However, the reusability of the nanoparticles for the purpose of sensing needs to be tested in the laboratory condition. The volume being handled, including other consumables used for sensing, is small, and therefore, potential environmental risk is minimized.

https://dx.doi.org/10.1021/acsomega.0c03465
ACS Omega 2020, 5, 25253−25263

2.6. Practical Aspects. The cost of detection was estimated to be 7 cents/10 assay, and the smartphone attachment is estimated to cost US$ 5 (excluding the phone), which taken together is orders of magnitude less expensive than commercial fluoride sensors. Major advantage of this nanoparticle-based sensor is that it minimizes the amount of reagents and sample consumption needed for each test, thereby reducing waste generation. Using the catalytic platform imparted by the nanoparticles, a LOD of 0.06 ppm was achieved. Metal-oxide nanoparticles are easy to handle, as they are stable entities and exhibit higher shelf-life. Further, the process does not involve the use of extra buffer media or corrosive acids, toxic chemicals like sodium arsenite to remove interference, and avoids mixed solvent systems to accelerate sensor performance. All of these make it simple and user-friendly compared to the commercially available F^- test kits. Moreover, this device does not involve purchase of any expensive display interface dedicated only to F^- measurement. The smartphone app and sensor extension are built in a way such that they can be modified easily for the detection of other contaminants, just by changing the active reagents.

3. CONCLUSIONS

In conclusion, we developed a cost-effective, field-deployable, and integrated sensing platform installed on a smartphone for fluoride detection and quantification with a high degree of sensitivity and specificity. The bicomponent sensing material was prepared using a mixture of near-cubic ceria−zirconia NC and XO dye, which rapidly changes color from yellow to red upon interaction with fluoride down to sub-ppm levels. The NCs have been thoroughly characterized for their properties and shelf life, and the sensing mechanism has been studied in detail by XPS and NMR spectroscopies. The sensing material has been tested against high concentrations of other common anions likely to be present in natural waters which gave negative results and proved its selectivity toward F^-. The smartphone reader was integrated to an external sensing attachment consisting of an LED and a photodiode-based optical setup for the estimation of the F^- content, having an LOD of 0.06 ppm. We demonstrated consistent performance of this portable sensor for simultaneous detection and quantification in environmental field water samples and various dental care products at a cost of less than 1 cent/assay. The aspects such as shape-dependent sensitivity and environmental impact of the nanomaterial used have been also explored.

4. EXPERIMENTAL SECTION

4.1. Materials. Zirconium oxychloride octahydrate ($ZrOCl_2{\cdot}8H_2O$), cerium nitrate hexahydrate ($CeNO_3{\cdot}6H_2O$), XO sodium salt (XO), and ethylene glycol were purchased from Loba Chemie, SRL chemicals and Merck, respectively. Ethanol was procured from Changshu Chemicals, while hydrochloric acid and sodium fluoride were supplied by Hi-media. All synthesis and control experiments were done using distilled water.

4.2. Methods. *4.2.1. Preparation of NCs.* The CeO_2@ZrO_2 core−shell NCs were synthesized by suitable modification of a reported procedure which involves the growth of ZrO_2 on the colloidal seed of CeO_2 nanoparticles.[31] 1 mL of 0.5 M cerium nitrate was mixed in 30 mL ethylene glycol and 3 mL water inside a hydrothermal bomb. The reaction mixture was heated at 180 °C for 12 h. After the temperature came down to room temperature, 0.3 mL of 0.5 M zirconium oxychloride is added and again heated at 180 °C for 8 h. The resultant solution was centrifuged at 5000 rpm for 5 min, washed, and redispersed in ethanol. NCs were characterized by TEM, FESEM, energy-dispersive spectroscopy (EDS), XPS, dynamic light scattering (DLS), and XRD techniques.

4.2.2. Preparation of XO Dye Solution. 2 mL of 1 mM XO solution in water was taken to which 20 μL of concentrated hydrochloric acid was added to obtain yellow color starting from violet. The acidified solution was kept undisturbed for 4 h and then diluted with water in 1:1 ratio.

4.2.3. Procedure for Colorimetric Sensing. Ethanolic dispersion of NCs and an acidic solution of the dye were mixed in 1:1 (v/v) ratio and added to 2.5 mL of F^--contaminated water to observe the color change from yellow to red. Same steps are followed for absorbance and device-based experiments. The sensor responses were compared with ISE results for field samples and dental care products.

4.3. Instrumentation. Absorbance spectra were measured using a PerkinElmer Lambda 365 instrument in the range of 200−1100 nm. TEM and high-resolution TEM (HRTEM) were performed at an accelerating voltage of 200 kV on a JEOL 3010, 300 kV instrument equipped with a UHR polepiece. The accelerating voltage was kept low to ensure that beam-induced damage on the material was low. The samples for HRTEM were prepared as dispersions which were drop-casted on carbon-coated copper grids and allowed to dry under ambient conditions. FESEM (Tescan-Mira 3 LMH) imaging was done in high vacuum and low vacuum (up to 500 Pa) conditions with accelerating voltage from 50 V to 30 kV and 20 ns to 10 ms per pixel scanning speed. EDS was done by using FEI Quanta 200, typically at 20 kV acceleration voltage. XPS measurements were done using an ESCA Probe TPD spectrometer of Omicron Nanotechnology. Polychromatic Mg Kα was used as the X-ray source ($h\nu$ = 1253.6 eV). Samples were spotted as drop-cast films on a sample stub. Constant analyzer energy of 20 eV was used for the measurements. Binding energy was calibrated with respect to C 1s at 284.8 eV. Residual fluoride concentration in water was measured (using TISAB) by a fluoride-ion selective electrode (ION 2700, Eutech Instruments). Device fabrication details are presented in the main text.

■ ASSOCIATED CONTENT

Supporting Information

The Supporting Information is available free of charge at https://pubs.acs.org/doi/10.1021/acsomega.0c03465.

Large-area TEM and FESEM of NC before and after F^- interaction, temperature-dependent kinetic plots for the interaction of NC−XO with F^-, IR spectra of NC−XO before and after interaction with F^-, absorbance plot of NC−XO response toward various fluoridated dental care products and the consequent standard curve, absorbance plot of NC−XO response toward F^- at different pH, full length overlapping ^{1}H NMR spectra of NC−XO before and after interaction with F^-, full length ^{1}H NMR spectrum of XO at high pH, workflow for using the F^- sensor app for sample measurement, and optical images of control experiments using with the zirconium−XO complex, ZrO_2 NP−XO, CeO_2 NP−XO, and spherical CeO_2@ZrO_2 NC−XO systems for 0, 0.1, 1, and 10 ppm of F^- (PDF)

https://dx.doi.org/10.1021/acsomega.0c03465
ACS Omega 2020, 5, 25253−25263

AUTHOR INFORMATION

Corresponding Author

Thalappil Pradeep − *DST Unit of Nanoscience (DST UNS) and Thematic Unit of Excellence (TUE), Department of Chemistry, Indian Institute of Technology Madras, Chennai 600036, India;* orcid.org/0000-0003-3174-534X; Phone: +91-44 2257 4208; Email: pradeep@iitm.ac.in; Fax: +91-44 2257 0545/0509

Authors

Sritama Mukherjee − *DST Unit of Nanoscience (DST UNS) and Thematic Unit of Excellence (TUE), Department of Chemistry and EWRE Division, Department of Civil Engineering, Indian Institute of Technology Madras, Chennai 600036, India*

Manav Shah − *DST Unit of Nanoscience (DST UNS) and Thematic Unit of Excellence (TUE), Department of Chemistry, Indian Institute of Technology Madras, Chennai 600036, India*

Kamalesh Chaudhari − *DST Unit of Nanoscience (DST UNS) and Thematic Unit of Excellence (TUE), Department of Chemistry, Indian Institute of Technology Madras, Chennai 600036, India*

Arijit Jana − *DST Unit of Nanoscience (DST UNS) and Thematic Unit of Excellence (TUE), Department of Chemistry, Indian Institute of Technology Madras, Chennai 600036, India*

Chennu Sudhakar − *DST Unit of Nanoscience (DST UNS) and Thematic Unit of Excellence (TUE), Department of Chemistry, Indian Institute of Technology Madras, Chennai 600036, India*

Pillalamarri Srikrishnarka − *DST Unit of Nanoscience (DST UNS) and Thematic Unit of Excellence (TUE), Department of Chemistry, Indian Institute of Technology Madras, Chennai 600036, India;* orcid.org/0000-0001-5187-6879

Md Rabiul Islam − *DST Unit of Nanoscience (DST UNS) and Thematic Unit of Excellence (TUE), Department of Chemistry, Indian Institute of Technology Madras, Chennai 600036, India*

Ligy Philip − *EWRE Division, Department of Civil Engineering, Indian Institute of Technology Madras, Chennai 600036, India;* orcid.org/0000-0001-8838-2135

Complete contact information is available at: https://pubs.acs.org/10.1021/acsomega.0c03465

Notes

The authors declare no competing financial interest.

ACKNOWLEDGMENTS

The authors thank Ramesh Kumar, IIT Madras, for helping to access 3-D printing facility; the Common facility, Department of Chemistry, IIT Madras, for pXRD and NMR measurements. The authors also thank the FESEM facility of CeNS, Bangalore, and Biswajit Mondal, IIT Madras, for TEM imaging. Authors thank the Department of Science and Technology, Government of India, for supporting our research program on nanotechnology for clean water.

REFERENCES

(1) Jagtap, S.; Yenkie, M. K.; Labhsetwar, N.; Rayalu, S. Fluoride in Drinking Water and Defluoridation of Water. *Chem. Rev.* **2012**, *112*, 2454−2466.

(2) Ayoob, S.; Gupta, A. K. Fluoride in Drinking Water: A Review on the Status and Stress Effects. *Crit. Rev. Environ. Sci. Technol.* **2006**, *36*, 433.

(3) *Fluoride in Drinking-Water Background Document for Development of WHO Guidelines for Drinking-Water Quality*; World Health Organization, 2004.

(4) National Research Council. *Fluoride in Drinking Water*; National Academies Press, 2006.

(5) Trieu, A.; Mohamed, A.; Lynch, E. Silver Diamine Fluoride versus Sodium Fluoride for Arresting Dentine Caries in Children: A Systematic Review and Meta-Analysis. *Sci. Rep.* **2019**, *9*, 1−9.

(6) Jia, B.; Zong, L.; Lee, J. Y.; Lei, J.; Zhu, Y.; Xie, H.; Clemens, J. L.; Feller, M. C.; Na, Q.; Dong, J.; et al. Maternal Supplementation of Low Dose Fluoride Alleviates Adverse Perinatal Outcomes Following Exposure to Intrauterine Inflammation. *Sci. Rep.* **2019**, *9*, 2575.

(7) Featherstone, J. D. B. Prevention and Reversal of Dental Caries: Role of Low Level Fluoride. *Community Dent. Oral Epidemiol.* **1999**, *27*, 31−40.

(8) Mao, S.; Chang, J.; Zhou, G.; Chen, J. Nanomaterial-Enabled Rapid Detection of Water Contaminants. *Small* **2015**, *11*, 5336−5359.

(9) Kim, H. N.; Guo, Z.; Zhu, W.; Yoon, J.; Tian, H. Recent Progress on Polymer-Based Fluorescent and Colorimetric Chemosensors. *Chem. Soc. Rev.* **2011**, *40*, 79−93.

(10) Bandodkar, A. J.; Wang, J. Non-Invasive Wearable Electrochemical Sensors: A Review. *Trends Biotechnol.* **2014**, *32*, 363−371.

(11) Gilardi, G.; Zhou, L. Q.; Hibbert, L.; Cass, A. E. G. Engineering the Maltose Binding Protein for Reagentless Fluorescence Sensing. *Anal. Chem.* **1994**, *66*, 3840−3847.

(12) Ji, H.-F.; Thundat, T.; Dabestani, R.; Brown, G. M.; Britt, P. F.; Bonnesen, P. V. Ultrasensitive Detection of CrO42- Using a Microcantilever Sensor. *Anal. Chem.* **2001**, *73*, 1572−1576.

(13) Guo, Y.; Li, J.; Chai, S.; Yao, J. Nanomaterials for the Optical Detection of Fluoride. *Nanoscale* **2017**, *9*, 17667−17680.

(14) Zhou, Y.; Zhang, J. F.; Yoon, J. Fluorescence and Colorimetric Chemosensors for Fluoride-Ion Detection. *Chem. Rev.* **2014**, *114*, 5511−5571.

(15) Du, J.; Jiang, L.; Shao, Q.; Liu, X.; Marks, R. S.; Ma, J.; Chen, X. Colorimetric Detection of Mercury Ions Based on Plasmonic Nanoparticles. *Small* **2013**, *9*, 1467−1481.

(16) Liu, Y.; Ai, K.; Cheng, X.; Huo, L.; Lu, L. Gold-Nanocluster-Based Fluorescent Sensors for Highly Sensitive and Selective Detection of Cyanide in Water. *Adv. Funct. Mater.* **2010**, *20*, 951−956.

(17) George, A.; Shibu, E. S.; Maliyekkal, S. M.; Bootharaju, M. S.; Pradeep, T. Luminescent, Freestanding Composite Films of Au 15 for Specific Metal Ion Sensing. *ACS Appl. Mater. Interfaces* **2012**, *4*, 639−644.

(18) Saha, K.; Agasti, S. S.; Kim, C.; Li, X.; Rotello, V. M. Gold Nanoparticles in Chemical and Biological Sensing. *Chem. Rev.* **2012**, *112*, 2739−2779.

(19) Liu, B.; Huang, Z.; Liu, J. Boosting the Oxidase Mimicking Activity of Nanoceria by Fluoride Capping: Rivaling Protein Enzymes and Ultrasensitive F- Detection. *Nanoscale* **2016**, *8*, 13562−13567.

(20) Guo, Y.; Zhang, L.; Zhang, S.; Yang, Y.; Chen, X.; Zhang, M. Fluorescent Carbon Nanoparticles for the Fluorescent Detection of Metal Ions. *Biosens. Bioelectron.* **2015**, *63*, 61−71.

(21) Ebrahim, F. M.; Nguyen, T. N.; Shyshkanov, S.; Gładysiak, A.; Favre, P.; Zacharia, A.; Itskos, G.; Dyson, P. J.; Stylianou, K. C. Selective, Fast-Response, and Regenerable Metal-Organic Framework for Sampling Excess Fluoride Levels in Drinking Water. *J. Am. Chem. Soc.* **2019**, *141*, 3052.

(22) Hu, J.; Dai, L.; Liu, S. Analyte-Reactive Amphiphilic Thermoresponsive Diblock Copolymer Micelles-Based Multifunctional Ratiometric Fluorescent Chemosensors. *Macromolecules* **2011**, *44*, 4699−4710.

(23) Xu, R.-X.; Yu, X.-Y.; Gao, C.; Jiang, Y.-J.; Han, D.-D.; Liu, J.-H.; Huang, X.-J. Non-Conductive Nanomaterial Enhanced Electrochemical Response in Stripping Voltammetry: The Use of Nanostructured Magnesium Silicate Hollow Spheres for Heavy Metal Ions Detection. *Anal. Chim. Acta* **2013**, *790*, 31−38.

(24) Melaimi, M.; Gabbaï, F. P. A Heteronuclear Bidentate Lewis Acid as a Phosphorescent Fluoride Sensor. *J. Am. Chem. Soc.* **2005**, *127*, 9680−9681.
(25) Bellack, E.; Schouboe, P. J. Rapid Photometric Determination of Fluoride in Water: Use of Sodium 2-(p-Sulfophenylazo)-1,8-Dihydroxynaphthalene-3,6-Disulfonate-Zirconium Lake. *Anal. Chem.* **1958**, *30*, 2032−2034.
(26) SPADNS Zirconium Lake method. https://www3.epa.gov/ttnemc01/qahandbook3/qaiii1977/qavoliii-aug1977-sec3-10.pdf (accessed March 26, 2020).
(27) Fluoride Test Kit Method. http://www.thermo.com.cn/Resources/201307/9131927687.pdf (accessed March 26, 2020).
(28) Hussain, I.; Ahamad, K. U.; Nath, P. Low-Cost, Robust, and Field Portable Smartphone Platform Photometric Sensor for Fluoride Level Detection in Drinking Water. *Anal. Chem.* **2017**, *89*, 767−775.
(29) Levin, S.; Krishnan, S.; Rajkumar, S.; Halery, N.; Balkunde, P. Monitoring of Fluoride in Water Samples Using a Smartphone. *Sci. Total Environ.* **2016**, *551*−*552*, 101−107.
(30) Balan Pillai, A.; Varghese, B.; Madhusoodanan, K. N. Design and Development of Novel Sensors for the Determination of Fluoride in Water. *Environ. Sci. Technol.* **2012**, *46*, 404−409.
(31) Liang, X.; Wang, X.; Zhuang, Y.; Xu, B.; Kuang, S.; Li, Y. Formation of CeO2-ZrO2 Solid Solution Nanocages with Controllable Structures via Kirkendall Effect. *J. Am. Chem. Soc.* **2008**, *130*, 2736−2737.
(32) Yuchi, A.; Hokari, N.; Wada, H.; Nakagawa, G. Semi-xylenol orange complex of zirconium(IV) as a photometric reagent system for fluoride based on mixed ligand complex formation. *Analyst* **1993**, *118*, 219−222.
(33) Wang, J.; Xu, W.; Chen, L.; Jia, Y.; Wang, L.; Huang, X.-J.; Liu, J. Excellent Fluoride Removal Performance by CeO2-ZrO2 Nanocages in Water Environment. *Chem. Eng. J.* **2013**, *231*, 198−205.
(34) Devaiah, D.; Reddy, L. H.; Park, S.-E.; Reddy, B. M. Ceria−Zirconia Mixed Oxides: Synthetic Methods and Applications. *Catal. Rev.* **2018**, *60*, 177−277.
(35) Belleza, O. J. V.; Villaraza, A. J. L. Ion Charge Density Governs Selectivity in the Formation of Metal-Xylenol Orange (M-XO) Complexes. *Inorg. Chem. Commun.* **2014**, *47*, 87−92.
(36) Handbook of Surface and Interface Analysis: Methods for Problem-Solving. https://books.google.co.in/books?id=2F3QKUBZfAC&pg=PA169&lpg=PA169&dq=ce+4f+levels+overlaps+with+o+2p+orbitals&source=bl&ots=7jtEdF1XNs&sig=ACfU3U1ikqhQEIOFFEZwwFRPGh9rlYQlQ&hl=en&sa=X&ved=2ahUKEwjzdfR65ToAhVC4jgGHatiCL8Q6AEwA3oECAgQAQ#v=onepage&q=ce4flevelsoverlapswitho2porbitals&f=false (accessed March 12, 2020).
(37) Maslakov, K. I.; Teterin, Y. A.; Ryzhkov, M. V.; Popel, A. J.; Teterin, A. Y.; Ivanov, K. E.; Kalmykov, S. N.; Petrov, V. G.; Petrov, P. K.; Farnan, I. The Electronic Structure and the Nature of the Chemical Bond in CeO2. *Phys. Chem. Chem. Phys.* **2018**, *20*, 16167.
(38) Shoko, E.; Smith, M. F.; McKenzie, R. H. Mixed Valency in Cerium Oxide Crystallographic Phases: Valence of Different Cerium Sites by the Bond Valence Method. *Phys. Rev. B: Condens. Matter Mater. Phys.* **2009**, *79*, 134108.
(39) MIT App Inventor|Explore MIT App Inventor. https://appinventor.mit.edu/ (accessed March 12, 2020).
(40) Daines, T. L.; Morse, K. W. A Spectrophotometric Determination of Fluoride Adapted for the Freshman Laboratory. *J. Chem. Educ.* **1974**, *51*, 680−681.
(41) Reshetnyak, V. Y.; Nesterova, O. V.; Admakin, O. I.; Dobrokhotov, D. A.; Avertseva, I. N.; Dostdar, S. A.; Khakimova, D. F. Evaluation of Free and Total Fluoride Concentration in Mouthwashes via Measurement with Ion-Selective Electrode. *BMC Oral Health* **2019**, *19*, 251.
(42) Gu, J.-A.; Lin, Y.-J.; Chia, Y.-M.; Lin, H.-Y.; Huang, S.-T. Colorimetric and bare-eye determination of fluoride using gold nanoparticle agglomeration probes. *Microchim. Acta* **2013**, *180*, 801−806.
(43) Sun, J.-F.; Liu, R.; Zhang, Z.-M.; Liu, J.-F. Incorporation of the fluoride induced SiO bond cleavage and functionalized gold nanoparticle aggregation into one colorimetric probe for highly specific and sensitive detection of fluoride. *Anal. Chim. Acta* **2014**, *820*, 139−145.
(44) Madhuprasad; Nityananda Shetty, A.; Trivedi, D. R. Colorimetric receptors for naked eye detection of inorganic fluoride ion in aqueous media using ICT mechanism. *RSC Adv.* **2012**, *2*, 10499−10504.
(45) Kumar, A.; Bhatt, M.; Vyas, G.; Bhatt, S.; Paul, P. Sunlight Induced Preparation of Functionalized Gold Nanoparticles as Recyclable Colorimetric Dual Sensor for Aluminum and Fluoride in Water. *ACS Appl. Mater. Interfaces* **2017**, *9*, 17359−17368.
(46) Nishimura, T.; Xu, S.-Y.; Jiang, Y.-B.; Fossey, J. S.; Sakurai, K.; Bull, S. D.; James, T. D. A simple visual sensor with the potential for determining the concentration of fluoride in water at environmentally significant levels. *Chem. Commun.* **2013**, *49*, 478−480.
(47) Liu, B.; Huang, Z.; Liu, J. Boosting the oxidase mimicking activity of nanoceria by fluoride capping: Rivaling protein enzymes and ultrasensitive F- detection. *Nanoscale* **2016**, *8*, 13562−13567.
(48) Li, Y.; Duan, Y.; Zheng, J.; Li, J.; Zhao, W.; Yang, S.; Yang, R. Self-assembly of graphene oxide with a silyl-appended spiropyran dye for rapid and sensitive colorimetric detection of fluoride ions. *Anal. Chem.* **2013**, *85*, 11456−11463.
(49) http://www.hach.com/pocket-colorimeter-ii-fluoridespadns-ii-arsenic-free/product-details?id=7640445206 (accessed 2020-03-27).
(50) Dahle, J.; Arai, Y. Environmental Geochemistry of Cerium: Applications and Toxicology of Cerium Oxide Nanoparticles. *Int. J. Environ. Res. Public Health* **2015**, *12*, 1253−1278.
(51) *Chemical Information Profile for Ceric Oxide Supporting Nomination for Toxicological Evaluation by the National Toxicology Program*, 2006.
(52) Nyoka, M.; Choonara, Y. E.; Kumar, P.; Kondiah, P. P. D.; Pillay, V. Synthesis of Cerium Oxide Nanoparticles Using Various Methods: Implications for Biomedical Applications. *Nanomaterials* **2020**, *10*, 242.
(53) Issa Hamoud, H.; Azambre, B.; Finqueneisel, G. Reactivity of Ceria−Zirconia Catalysts for the Catalytic Wet Peroxidative Oxidation of Azo Dyes: Reactivity and Quantification of Surface Ce(IV)-Peroxo Species. *J. Chem. Technol. Biotechnol.* **2016**, *91*, 2462−2473.

https://dx.doi.org/10.1021/acsomega.0c03465
ACS Omega 2020, 5, 25253−25263